Available online at www.sciencedirect.com

ScienceDirect

Proceedings of the Combustion Institute 37 (2019) 841–848

Proceedings of the Combustion Institute

www.elsevier.com/locate/proci

Soot aggregate morphology in coflow laminar ethylene diffusion flames at elevated pressures

Ben Gigone, Ahmet E. Karataş, Ömer L. Gülder*

University of Toronto Institute for Aerospace Studies, 4925 Dufferin Street, Toronto, Ontario M3H 5T6, Canada

Received 29 November 2017; accepted 13 June 2018
Available online 29 June 2018

Abstract

The effect of combustion pressure on soot aggregate morphology and on primary soot particle diameter was investigated by thermophoretic sampling in nitrogen-diluted ethylene flames. Soot aggregate samples were collected using a high-pressure thermophoretic sampling system installed inside the high-pressure combustion chamber. Collected samples were imaged by transmission electron microscopy followed by an automated image analysis process to yield aggregate morphology information. The experiments covered pressures from 3 to 6 bar, and samples were collected at heights of 2 and 5 mm above the burner exit in nitrogen-diluted ethylene (ethylene to nitrogen mole ratio 2:1) flames with nominal visible flame heights of about 20 mm. It was observed that average primary soot particle diameter increased with increasing pressure within the pressure range considered, at both measurement locations within the flame. Fractal parameters of the soot aggregates were inferred directly from the experimental data (as opposed to the usual practice of assuming *a priori* values for fractal dimension and pre-factor). Near to the soot nucleation and growth regions of the co-flow laminar diffusion flames, at 2 mm above the burner exit, the fractal dimension of the aggregates was not as high as the accepted universal value of about 1.9, in spite of the fact that number of primary particles per aggregate is quite high and pressure is well above atmospheric. At 5 mm above the burner exit, however, the fractal dimension of the soot aggregates approached the accepted universal value of 1.9, at high pressures; at relatively lower pressures, the fractal dimension was about 1.6 at the same location within the flame. In view of the inferred fractal results, caution should be exercised when applying fractal analysis to low heights in flames at lower pressures where soot inception and growth are relatively dominant.

Keywords: Soot morphology at pressure; High-pressure soot formation; Fractal characteristics of soot; Primary soot size distribution

1. Introduction

Combustion generated soot, also known as particulate matter in transportation technology and black carbon in atmospheric sciences, is an artefact of non-premixed and rich premixed modes of

* Corresponding author.
E-mail address: ogulder@utias.utoronto.ca (Ö.L. Gülder).

https://doi.org/10.1016/j.proci.2018.06.103
1540-7489

combustion of fossil and biomass derived fuels. In addition to its contribution to climate change, exposure to soot is responsible for severe health effects on humans. The morphology and structure of the combustion generated soot aggregates have shown to have a significant influence on the optical and radiative transfer properties of these carbonaceous particles [1–3]. The light scattering and absorbtion characteristics of soot aggregates, for example, are dependent on the aggregate morphology [4].

The linkages between radiative/optical properties and soot aggregate morphology have inspired extensive research efforts in this area for a broad range of applications such as optical diagnostics developments for combustion and industrial aerosol processes [4,5], to estimate the continuum radiation and heterogeneous reaction properties of soot in flame environments [6], in addition to environmental issues, remote sensing, and astrophysical phenomena involving light propagation and scattering. Power laws applicable to soot aggregates can be interpreted as being related to fractal-like structures. Fractal-like objects whose shapes vary seemingly irregularly in the classical geometric sense from one to another, but possess certain similarities statistically; they display self-similar and scale invariant behaviour over certain length scales. The concept of a soot aggregate having fractal characteristics with a fractal dimension (Hausdorf dimension) makes it possible to describe the complex geometry using a statistical scaling law first proposed by Forrest and Witten [7]. For fractal clusters with N primary soot particles of diameter d_p, the radius of gyration R_g can be shown to be related to the primary particle diameter by

$$N = k_f \left(\frac{2R_g}{d_p} \right)^{D_f} \tag{1}$$

where k_f is the pre-fractal factor and D_f is the fractal dimension of the subject soot aggregate. It is argued that D_f is universal for combustion generated soot aggregates. Near the soot inception point within the flames the aggregates are relatively small having a few primary particles, but they grow rapidly containing several hundred primary particles per aggregate by the time soot concentrations reach their maximum levels [1,8].

Majority of the soot aggregate morphology studies, reported in the literature, are related to the over-fire soot [9,10], soot emitted from the combustion devices, or in-cylinder sampling in diesel combustion [11,12]. Investigations tracking the evolution of soot aggregate morphology within the flames are limited and mostly carried out in atmospheric flames, see e.g. [8,13,14]. Unraveling the sensitivity of soot processes to elevated pressures is important because combustion devices used in transportation operate at high pressures and it has been shown that the pressure has a significant influence on soot processes [15]. However, the rate determining chemical reactions of combustion, including those involved in soot processes, are nonlinear in nature, and as a result the sensitivity of combustion events to changes in pressure are not usually monotonic. Consequently, it is a problematic issue to project the results inferred from experimental measurements in atmospheric flames to high-pressure combustion with confidence.

Recent advancements in experimental apparatus design have allowed for the physical collection and analysis of soot aggregates in high-pressure laminar diffusion flames [16–18]. While a number of non-intrusive measurement techniques have been popular in previous soot studies, the desire for information regarding soot morphology [19] (and, particularly, soot fractal parameters) calls for intrusive measurement techniques. For the measurement of primary soot particle size, soot aggregate information, soot fractal dimension, and soot concentration in atmospheric flames, laser scattering and extinction techniques have provided reliable results [20–22]. However, issues arise as pressure is increased, as light extinction and spectral soot emission techniques, while successful in soot concentration and temperature measurements [15], have not been demonstrated to provide reliable soot morphology and primary soot particle size information.

A number of thermophoretic soot sampling studies, with subsequent TEM (transmission electron microscopy) imaging, have been used successfully to measure primary soot particle size and relevant soot morphology parameters in laminar diffusion flames at atmospheric pressure [13,23–26]. Recently, a thermophoretic sampling system capable of collecting physical soot samples at high pressures was developed [17,27]. This recent development allows for the collection and comparison of soot morphology information as pressure is varied across a number of vertical flame height sampling positions in a laminar diffusion flame.

Current implementations of simultaneous light scattering and extinction techniques require that the fractal dimension and the pre-factor should be known *a priori* to infer the primary soot particle size and aggregate properties from optical measurements [28]. Assuming a set of values for D_f and k_f representative of a wide range of flame conditions would be fine for fully developed soot aggregates, but for those developing aggregates close to the soot nucleation regions it is expected that the values of D_f and k_f would be changing along the soot formation and aggregate growth path. Although the laser-induced incandescence (LII) has been used with success to measure primary soot particle size and concentration at atmospheric conditions [29,30], its use at elevated pressures for primary soot particle size (and aggregate morphology) has encountered several challenges [16,31,32]. Due to these uncertainties involved in optical techniques

in high pressure flames, thermophoretic sampling combined with TEM analysis seem to be a logical choice to study the influence of pressure on soot aggregate morphology in tractable flames.

The objective of this study was to investigate the evolution of the soot aggregate morphology in nitrogen-diluted ethylene flames at pressures up to 6 bar. We used a thermophoretic soot sampling system with multiple probes mounted into a high-pressure combustion chamber, capable of stabilizing laminar diffusion flames at high pressures, for collecting soot samples on TEM grids. Soot aggregate morphology, as a function of pressure, was inferred from the subsequent analysis of these TEM images. Primary soot particle size and aggregate morphology, including fractal dimension, at various pressures and axial locations in the flame are presented and discussed.

2. Experimental methodology

The nitrogen-diluted ethylene flames were stabilized in a high-pressure combustion chamber which had been used previously for high-pressure soot studies and have been described in detail in our previous publications [33–40]. Only a brief account of the chamber and the burner will be given here emphasizing its main features. The cylindrical combustion chamber has an internal diameter of 24 cm and a wall thickness of 18.2 mm. The internal height of the chamber is 60 cm. It is fitted with three radial observation ports mounted at 0°, 90°, and 180° that provide optical access to the chamber for various non-intrusive measurements. The high pressure chamber is installed on a translational stage which is driven by three stepper motors that can move the chamber in three dimensions with a precision of 5 μm. A circular coflow laminar diffusion flame burner with a fuel nozzle exit diameter of 3 mm and a coflow air nozzle with a diameter of 25 mm, installed inside the high pressure combustion chamber, was used. The exit rim of this stainless steel burner is tapered to a fine edge to prevent the formation of any recirculation zones. To provide uniform velocity profiles at the exit of the burner upstream of fuel and air nozzles are fitted with porous metal inserts. A schematic view of the experimental set up is shown in Fig. 1.

To take physical samples from high pressure flames, a thermophoretic sampling apparatus was designed and installed in the high pressure chamber, Fig. 2. The sampling apparatus has a circular sampling disk, a motor drive, and a control unit to program the sampling sequences. The circular sampling disk has ten arms extending radially, each housing a pocket to hold a 3 mm TEM grid at the end of the probe arm. Each pocket measures 3.3 mm in diameter, has a depth of 0.5 mm, and has 2.5 mm slot that exposes the mesh of the TEM grid to the flame. The further details of the

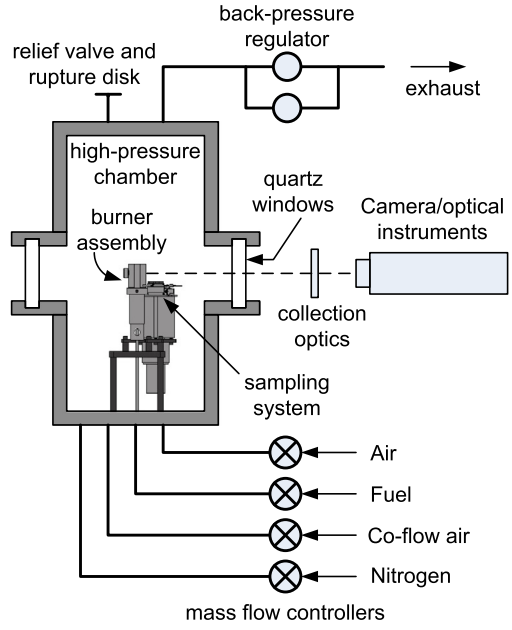

Fig. 1. A schematic view of the experimental setup.

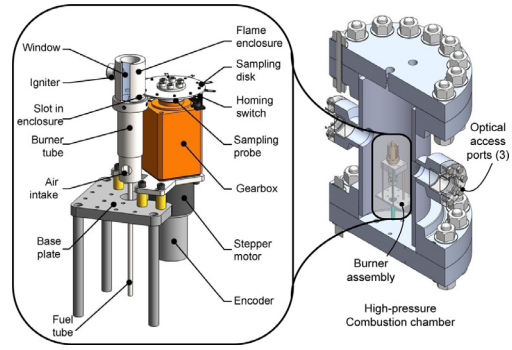

Fig. 2. Isometric view of the sampling system and the burner assembly along with a cut view of the high pressure chamber.

thermophoretic sampling apparatus have been reported previously and can be found in [17,27].

The sampling timing is controlled by the programmable control system of the sampling unit. The residence time, i.e. the time period during which the TEM grid stays within the flame at the sampling location, and the velocity of the sampling arm can be programmed as desired. For example, the probe arm can be programmed to decelerate as it enters the flame and reach a zero velocity when the TEM grid is at the desired sampling location. After the prescribed sampling time, the probe accelerates and exits the flame. In cases that soot aggregate information averaged over the flame cross-section is chosen, the

probe arm can be programmed to sweep across the flame cross-section at a constant angular velocity. To begin the sampling sequence, the stepper motor drives the circular sampling disk at the prescribed velocity profile and the sampling probe arms rotate through the slot in the flame enclosure. To take samples from different heights, the flame enclosure is vertically adjusted to the desired height or replaced with an enclosure with sampling slots at different heights. After each probe arm completes the sampling process, the sampling disk is slowed down or brought to a complete stop to allow the flame to recover from the disturbance, due to physical intrusion into the flame, and to have a stable flame for the next sampling process. Further details of the sampling system and procedure are given in [17].

Ethylene, nitrogen, and compressed air used in the study are of research grade purity. Thermal mass flow controllers (Brooks SLA5850) were calibrated for the desired flow rates using a positive displacement type calibration unit (MesaLabs Bios DryCal Definer 220). Ethylene is diluted with nitrogen (ethylene to nitrogen mole ratio 2:1) to prevent smoking flames at elevated pressures. Mass flow rate of ethylene was kept constant at 0.96 mg/s at all pressures to have tractable measurements. Co-flow air mass flow was kept constant at 0.34 g/s at all pressures. Keeping the fuel mass flow rate constant insures that the residence times of the flames do not change with pressure, and the measurements can be compared at a given flame height within the flames at different pressures. Experiments were conducted at pressures up to 6 bar and the sampling was confined to heights at 2 mm and 5 mm above the burner rim.

Typical examples of TEM images are shown in Fig. 3. To retrieve the desired parameters of the collected soot aggregates from TEM images, an automated image detection and evaluation method, adapted from Wang et al. [41] and Kook et al. [42], was employed. The sequence of image processing, as described by Wang et al. [41], starts with the application of median filtering, self-inversion, and self-subtraction schemes for the purpose of reducing image noise. The variability in the image background is taken into account and it is ensured that the details of the soot aggregates were not significantly compromised. An edge detection method, Canny Edge Detection, is then coupled with a modified Circular Hough Transform algorithm, to make sure that the features from both the internal and peripheral regions of the soot aggregates can be used for the identification of primary particles within the aggregates. Although the modified Circular Hough Transform algorithm requires from the user a sensitivity factor and primary particle diameter range, it was shown that it yields accurate estimates and is efficient computationally. To enable the automated aggregate characterization process, morphological closing operation is carried out such that each of the aggregates can be identified as a single object. Additionally, methods were included to calculate the radius of gyration of the projected aggregate images of the collected soot samples. For estimation of the radius of gyration of the aggregates the approximation proposed by Lapuarta et al. [43] was adapted. A subset of the TEM images was processed manually to check the validity of the automated image processing method we used and excellent agreement between the two was obtained. The details of the manual TEM image processing procedure used here for comparison are documented by Vargas [44].

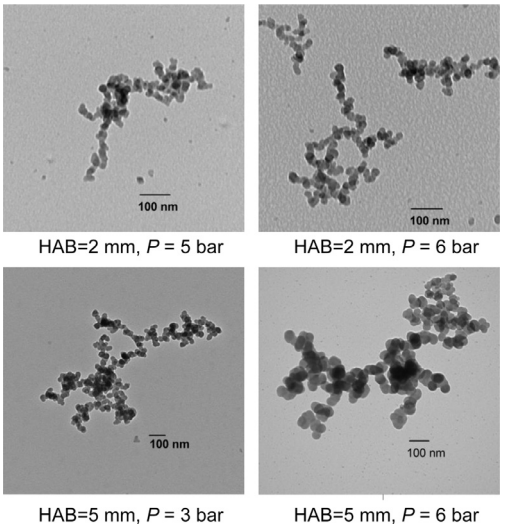

Fig. 3. Typical examples of TEM images of soot particles taken at 2 mm (top row) above the burner at 5 and 6 bar, and at 5 mm (lower row) at 3 and 6 bar. Solid bars on the images represent 100 nm.

3. Results and discussion

As the pressure is increased, the shape of the laminar diffusion flame gets more slender and the characteristic flame cross-sectional area at a given location on the flame centerline scales with the inverse of pressure [15,36]. Still pictures of flames at various pressures displayed shapes similar to those observed previously at elevated pressures.

Measured primary soot diameter distributions at 2 mm above the burner exit at 3, 4, 5, and 6 bar are shown as histograms in Fig. 4. Primary particle sizes were obtained by measuring the diameters, by the automated method described in the Experimental Methodology Section, of several thousands of particles in high-magnification images. In this nitrogen-diluted ethylene flame at 2 mm height above the burner exit, the mean primary soot particle diameter increases from 17 nm at 3 bar to 24 nm at 6 bar, Fig. 4. This is in contrast to our previous

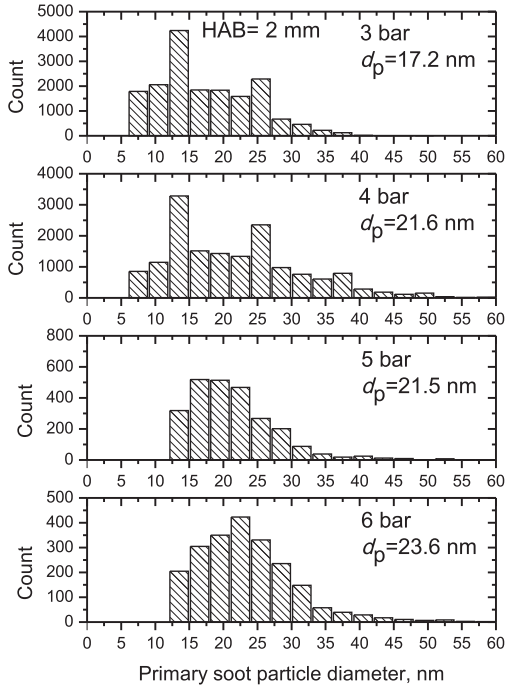

Fig. 4. Primary soot particle diameter distributions at 3, 4, 5, and 6 bar, at a height of 2 mm above the burner exit.

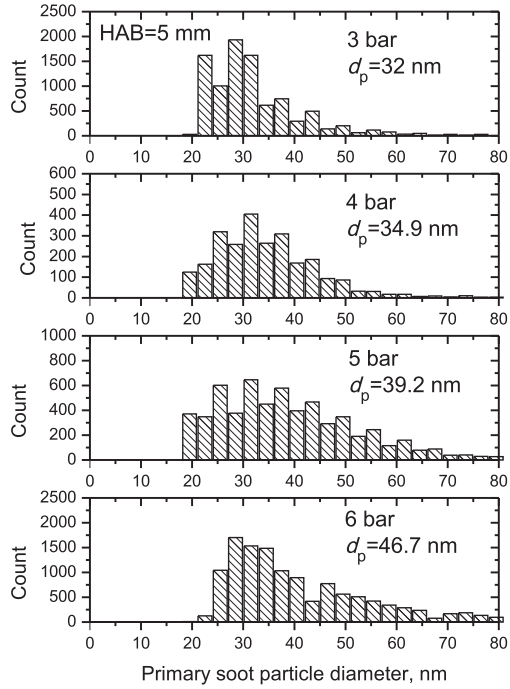

Fig. 5. Primary soot particle diameter distributions at 3, 4, 5, and 6 bar, at a height of 5 mm above the burner exit.

study of methane flames in which the primary soot particle diameter decreased with pressure at a height of 3 mm above the burner [27]. However, in the methane study the carbon mass flow of the fuel was one-half of the carbon mass flow rate in the current study, and methane and ethylene have quite different sooting characteristics. Further, primary particle size distributions at 2 mm above the burner do not display typical normal shapes at 3 and 4 bar pressures. This can be attributed to the fact that 2 mm height above the burner is where soot inception is still in progress. At the height of 5 mm above the burner, the size distribution histogram at pressures from 3 to 6 bar display a similar trend; the primary soot particle diameter increases from 32 nm at 3 bar to 47 nm at 6 bar pressure, Fig. 5. The maximum soot volume fractions in nitrogen-diluted ethylene flames at 2 mm height above the burner exit measured by soot spectral emission techniques showed a factor of about 6 increase in soot concentration from 3 to 6 bar, whereas the increase in mean primary soot particle diameter is about 40% within the same pressure range. Since soot volume fraction scales with the cube of the soot particle diameter, soot number density should be increasing in proportion to pressure. This implies that the number of nuclei formation increases with pressure. If the soot nucleation is mainly dominated by the collision of smaller PAH molecules (such as pyrene or higher), this process yields increasing number of nuclei as the pressure increases.

Typical soot aggregate size distributions, determined from the TEM images, are depicted in Fig. 6. At 2 mm above the burner exit at 5 bar the number of primary soot particles per aggregate are between 5 and 50 peaking at about 20 particles. At the same pressure but at 5 mm above the burner, the number of particles ranges from 10 to about 150, Fig. 6. At the same height within the flame but at 3 bar, aggregate size distribution is similar to the one at 5 bar. It is obvious that soot cluster sizes grow significantly with height above the burner exit from 2 mm to 5 mm.

The number of primary particles per aggregate, N, determined through the automated image processing, is plotted against the corresponding normalized radius of gyration, $2R_g/d_p$, according to Eq. (1) in Figs. 7 and 8 at a height of 2 mm above the burner exit, and in Figs. 9–11 at a height of 5 mm above the burner exit.

There are two important findings that are apparent in Figs. 7–10. First, the fractal dimensions of the soot aggregates in the soot formation and growth region of the co-flow laminar diffusion flames, at 2 mm above the burner exit, is not as high as the accepted universal value of about 1.9; they are relatively smaller, about 1.2, at 5 bar and increasing slightly with increasing pressure to 6 bar, Figs. 7 and 8. Second observation is that fractal

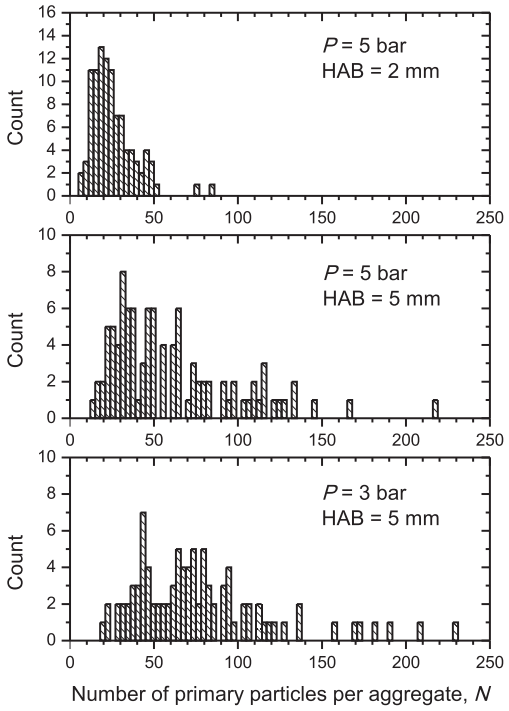

Fig. 6. Soot aggregate size distributions at heights of 2 mm (at 5 bar) and 5 mm (at 5 and 3 bar) above the burner exit.

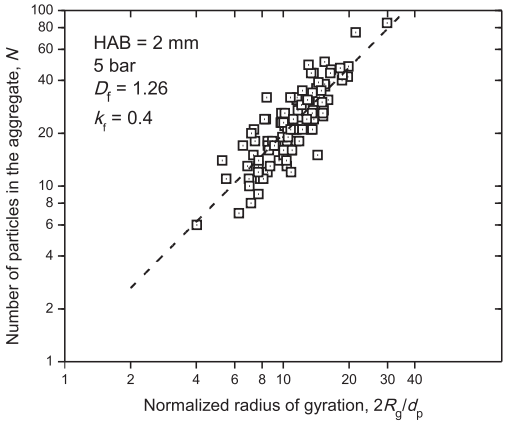

Fig. 7. Logarithmic plot of number of primary soot particles in an aggregate versus the normalized radius of gyration of the aggregate at 5 bar pressure and HAB = 2 mm. The slope of the best fit line yields the fractal dimension, D_f, per Eq. (1). k_f is the fractal prefactor.

dimension does not attain the universal value lower in the flame unless the pressure is high, Figs. 9–11. At 3 and 5 bar, at the axial height of 5 mm above the burner exit, fractal dimension is about 1.6, and it reaches 1.96 when the pressure is increased to 6 bar. Further at the height of 2 mm above the burner exit,

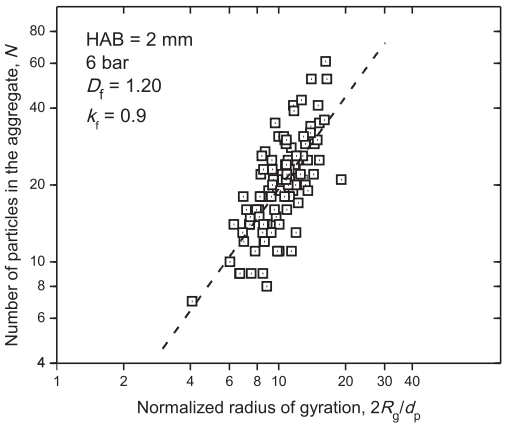

Fig. 8. Logarithmic plot of number of primary soot particles in an aggregate versus the normalized radius of gyration of the aggregate at 6 bar pressure and HAB = 2 mm. The slope of the best fit line yield the fractal dimension, D_f, per Eq. (1). k_f is the fractal prefactor.

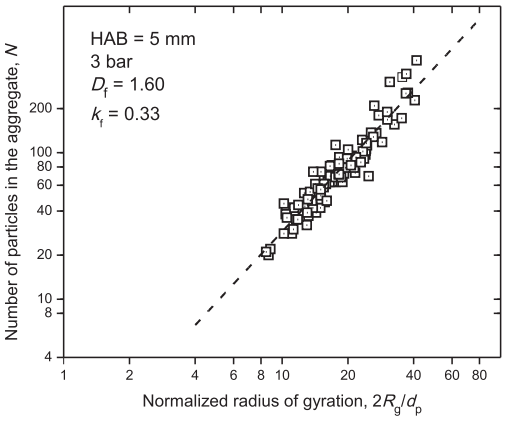

Fig. 9. Logarithmic plot of number of primary soot particles in an aggregate versus the normalized radius of gyration of the aggregate at 3 bar pressure and HAB = 5 mm. The slope of the best fit line yields the fractal dimension, D_f, per Eq. (1). k_f is the fractal prefactor.

the number of primary soot particles per aggregate is from about 6 to 80 at 5 and 6 bar, Figs. 7 and 8. On the other hand, N ranges from about 10 to several hundreds at a height of 5 mm above the burner exit, Figs. 9–11. It should be noted that TEM images of soot, sampled at 2 mm height and at pressures lower than 4 bar, displayed aggregates with mostly single digit number of primary particles. These images yielded fractal dimensions smaller than 1.2.

It is convenient for non-intrusive measurements of soot aggregate morphology to assume constant fractal parameters, see e.g. [28]. However, our current results strongly suggest that, in high pressure flames, the fractal analysis may not be meaningful

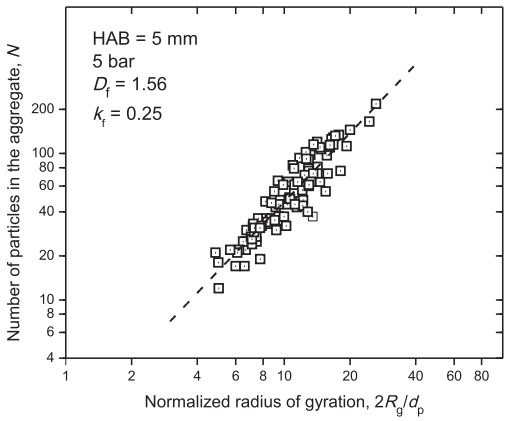

Fig. 10. Logarithmic plot of number of primary soot particles in an aggregate versus the normalized radius of gyration of the aggregate at 5 bar pressure and HAB = 5 mm. The slope of the best fit line yield the fractal dimension, D_f, per Eq. (1). k_f is the fractal prefactor.

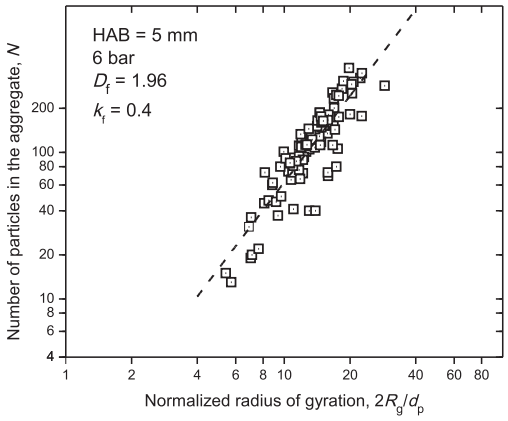

Fig. 11. Logarithmic plot of number of primary soot particles in an aggregate versus the normalized radius of gyration of the aggregate at 6 bar pressure and HAB = 5 mm. The slope of the best fit line yield the fractal dimension, D_f, per Eq. (1). k_f is the fractal prefactor.

at lower pressures and at flame locations near to soot inception and growth.

Insertion of the sampling probe into the flame creates an interference and changes the flow field of the gases within the flame envelope. This aspect is one of the major drawbacks of the thermophoretic sampling in flames and quantification of the uncertainty introduced is not a trivial matter. As discussed by Lee et al. [45], the disturbance imposed by the sampling probe would be expected to be mostly hydrodynamic and the resulting change in the flow field will have some influence on the sampling process. The interference created by the sampling apparatus used in this study is documented with high-speed photographs during the sampling process and reported recently [17,27]. Similar to those reported previously for TEM imaging to measure primary soot particle size [24], the experimental and image analysis based uncertainty was estimated to be within 10% (95% confidence interval). It was further assumed that, to a first approximation, the thermophoretic force and velocity do not change significantly with the Knudsen number in the transition regime [46]; therefore any sampling bias that may be introduced due to changes in Knudsen number with pressure is neglected. The axial distribution of the temperature decreases with increasing pressure due to enhanced radiation heat loss. Any affect this change may have on thermophoresis and aggregation is neglected.

4. Conclusions

Soot aggregate morphology, including primary soot particle size, number of primary particles in an aggregate, radius of gyration of the aggregates, and fractal parameters, was inferred from the analysis of thermophoreticly collected samples in high pressure laminar diffusion flames of ethylene diluted with nitrogen. The analysis method included TEM imaging and processing the images through an automated procedure. The sampling was done at two heights above the burner exit; at 2 and 5 mm. Pressure range was from 3 to 6 bar. The experimental results conclude that: (1) Average primary soot particle diameter increases with increasing pressure; (2) Soot number density increase is proportional to pressure; (3) At 2 mm above the burner exit, the fractal dimension of the aggregates is much smaller than the accepted universal value, in spite of the fact that number of primary particles per aggregate is quite high; (4) At 5 mm above the burner exit, the fractal dimension of the soot aggregates approaches the accepted universal value of 1.9 at 6 bar; and (5) Fractal dimension of the soot aggregates increases with pressure and with axial height above the burner exit. Considering the variation of the fractal dimension with sampling location and pressure, one must be careful not to apply mature soot TEM analysis near the soot inception and growth regions at relatively lower pressures.

Acknowledgment

The authors thank the Natural Sciences and Engineering Research Council of Canada for a discovery grant (RGPIN-2017-06063) and the Ontario Research Fund for a Research Excellence Program grant (ORF RE07-034), awarded to the senior author, for the support of this research work.

References

[1] Ü.Ö. Köylü, G. Faeth, *J. Heat Transf.* 115 (2) (1993) 409–417.
[2] Ü.Ö. Köylü, G.M. Faeth, T.L. Farias, M.G. Carvalho, *Combust. Flame* 100 (1995) 621–633.
[3] F. Liu, C. Wong, D. Snelling, G. Smallwood, *Aerosol Sci. Technol.* 47 (2013) 1393–1405.
[4] C.M. Sorensen, *Aerosol Sci. Technol.* 35 (2) (2001) 648–687.
[5] F. Liu, B. Stagg, D. Snelling, G. Smallwood, *Int. J. Heat Mass Transf.* 49 (3–4) (2006) 777–788.
[6] G. Faeth, Ü.Ö. Köylü, *Combust. Sci. Technol.* 108 (4–6) (1995) 207–229.
[7] S.R. Forrest, T.A. Witten, *J. Phys. A: Math. Gen* 12 (1979) L109–L117.
[8] M. Lapuerta, J. Barba, A.D. Sediako, M.R. Kholghy, M.J. Thomson, *J. Aerosol Sci.* 111 (2017) 65–74.
[9] Ü.Ö. Köylü, G.M. Faeth, *Combust. Flame* 89 (1992) 140–156.
[10] Ü.Ö. Köylü, G.M. Faeth, *J. Heat Transf.* 116 (1994) 152–159.
[11] R. Ryser, T. Gerber, T. Dreier, *Combust. Flame* 156 (2009) 120–129.
[12] R. Zhan, S. Kook, *Environ. Sci. Technol.* 48 (2014) 8243–8250.
[13] R.A. Dobbins, C.M. Megaridis, *Langmuir* 3 (1987) 254–259.
[14] Ü.Ö. Köylü, G. Faeth, *J. Heat Transfer* 116 (4) (1994) 971–979.
[15] A.E. Karataş, Ö.L. Gülder, *Prog. Energy Combust. Sci.* 38 (2012) 818–845.
[16] M. Leschowski, T. Dreier, C. Schulz, *Z. Phys. Chem.* 229 (2015) 781–805.
[17] A.M. Vargas, Ö.L. Gülder, *Rev. Sci. Instrum.* 87(5) (2016) 055101.
[18] M. Altenhoff, C. Teige, M. Storch, S. Will, *Rev. Sci. Instrum.* 87 (2016) 125108.
[19] H.A. Michelsen, P.E. Schrader, F. Goulay, *Carbon* 48 (2010) 2175–2191.
[20] Ü.Ö. Köylü, G. Faeth, *J. Heat Transf.* 118 (2) (1996) 415–421.
[21] R. Puri, T.F. Richardson, R.J. Santoro, R.A. Dobbins, *Combust. Flame* 92 (1993) 320–333.
[22] C.M. Sorensen, J. Cai, N. Lu, *Langmuir* 8 (1992) 2064–2069.
[23] Ü.Ö. Köylü, C.S. McEnally, D.E. Rosner, L.D. Pfefferle, *Combust. Flame* 110 (1997) 494–507.
[24] B. Hu, B. Yang, Ü.Ö. Köylü, *Combust. Flame* 134 (2003) 93–106.
[25] B. Hu, Ü.Ö. Köylü, *Aerosol Sci. Technol.* 38 (10) (2004) 1009–1018.
[26] Ü.Ö. Köylü, Y. Xing, D.E. Rosner, *Langmuir* 11 (1995) 4848–4854.
[27] A.M. Vargas, Ö.L. Gülder, *Proc. Combust. Inst.* 36 (2017) 975–984.
[28] H.M.F. Amin, W.L. Roberts, *Proc. Combust. Inst.* 36 (1) (2017) 861–869.
[29] D.R. Snelling, F. Liu, G.J. Smallwood, Ö.L. Gülder, *Combust. Flame* 136 (2004) 180–190.
[30] D.R. Snelling, G.J. Smallwood, F. Liu, Ö.L. Gülder, *Appl. Opt.* 44 (31) (2005) 6773–6785.
[31] K.A. Thomson, D.R. Snelling, G.J. Smallwood, F. Liu, *Appl. Phys. B: Lasers Opt.* 83 (2006) 469–475.
[32] E. Cenker, G. Bruneaux, T. Dreier, C. Schulz, *Appl. Phys. B: Lasers Opt.* 119 (2015) 745–763.
[33] H.I. Joo, Ö.L. Gülder, *Proc. Combust. Inst.* 32 (2009) 769–775.
[34] Ö.L. Gülder, G. Intasopa, H.I. Joo, P.M. Mandatori, D.S. Bento, M.E. Vaillancourt, *Combust. Flame* 158 (2011) 2037–2044.
[35] H.I. Joo, Ö.L. Gülder, *Combust. Flame* 158 (2011) 416–422.
[36] P.M. Mandatori, Ö.L. Gülder, *Proc. Combust. Inst.* 33 (2011) 577–584.
[37] P.H. Joo, Ö.L. Gülder, *Energy Fuels* 26 (2012) 5462–5467.
[38] A.E. Karataş, G. Intasopa, Ö.L. Gülder, *Combus. Flame* 160 (2013) 1650–1656.
[39] P.H. Joo, M.R.J. Charest, C.P.T. Groth, Ö.L. Gülder, *Combust. Flame* 160 (2013) 1990–1998.
[40] F. Liu, A.E. Karataş, Ö.L. Gülder, M. Gu, *Combust. Flame* 162 (5) (2015) 2231–2247.
[41] C. Wang, Q.N. Chan, R. Zhan, et al., *J. Nanopart. Res.* 18 (2016) 127.
[42] S. Kook, R. Zhang, Q. Chan, et al., *SAE Int. J. Engines* 9 (2016) 279–296.
[43] M. Lapuerta, R. Ballesteros, F.J. Martos, *J. Colloid Interf. Sci.* 303 (2006) 149–158.
[44] A.M. Vargas, *Design and Development of a Thermophoretic Soot Sampling System for High-Pressure Laminar Diffusion Flames*, University of Toronto, 2016. Master's thesis.
[45] J. Lee, I. Altman, M. Choi, *J. Aerosol Sci.* 39 (5) (2008) 418–431.
[46] L. Talbot, R.K. Cheng, R.W. Schefer, D.R. Willis, *J. Fluid Mech.* 101 (1980) 737–758.